SO$_2$ adsorption and transformation on calcined NiAl hydrotalcite-like compounds surfaces: An *in situ* FTIR and DFT study

Ling Zhao[a], Xinyong Li[a,*], Ce Hao[a], Colin L. Raston[b]

[a] Key Laboratory of Industrial Ecology and Environmental Engineering and State Key Laboratory of Fine Chemical, School of Environmental Sciences and Technology, Dalian University of Technology, Dalian, 116024, China
[b] Centre for Strategic Nano-Fabrication, The University of Western Australia, 35 Stirling Highway, Crawley, WA 6009, Australia

ARTICLE INFO

ABSTRACT

Flower-like hydrotalcite-based NiAl mixed oxides with high surface area were synthesized by urea hydrolysis approach, and employed for SO$_2$ removal. The catalyst was well characterized by TGA, ICP, XRD, SEM, TEM and N$_2$ adsorption/desorption isotherm analyses. The calcined NiAlO showed excellent SO$_2$ adsorption and its adsorption equilibrium was of a type I isotherm, which significantly improved the adsorption performance for low-concentration SO$_2$. XPS and TPD methods were conducted to identify the sulfate species. Specifically, *in situ* Fourier transform infrared spectroscopy revealed that adsorbed SO$_2$ molecules formed surface bidentate binuclear sulfate. Density functional theory based computations interpreted the vibrational data associated with the NiAlO surface and confirmed that sulfate species adopted a binuclear bidentate binding configuration on the surface of NiAlO catalyst.

© 2012 Elsevier B.V. All rights reserved.

1. Introduction

Layered double hydroxides, also known as hydrotalcite-like materials, are peculiar inorganic materials which can capture and exchange anions [1]. The general formula of hydrotalcite-like compounds is $[M_{1-x}^{II}M_x^{III}(OH)_2]A_{x/n}^{n-} \cdot mH_2O$, where M^{II} and M^{III} are respectively divalent and trivalent cations, the value of the coefficient x is equal to the molar ratio $M^{III}/(M^{II}+M^{III})$, and A^{n-} is an anion with charge n [2]. The mixed oxides obtained by thermal decomposition of hydrotalcite-like precursors often display good activity because of their smaller crystallite, higher surface area, basic surface properties and structure memory effect [3,4]. As a result, these materials have a wide variety of applications in industry, including as additives in polymers, in biology and medicine, in catalysis, and in environmental remediation [4–7].

SO$_2$ emissions from coal-fired power plants have caused significant environmental and human health effects. Stringent environmental regulations limiting atmospheric SO$_2$ emissions encourage the research of more efficient ways to reduce them. Many new strategies have been proposed [8–11]. From an economical point of view, the better strategy for the control of SO$_2$ emissions is the addition of selective sorbents [12,13].

Mixed oxides from hydrotalcite-like compounds have proved to be good sulphur-transfer catalysts [14,15] since they offer a large SO$_2$ adsorption capacity by forming metal sulfates. A large number of experimental studies have been performed to acquire insight into the adsorption and transformation mechanism of SO$_2$ on the calcined hydrotalcite-like compounds. Centi and Perathoner have reported that a series of Cu–Al mixed oxides derived from hydrotalcite precursors showed significantly favorable SO$_x$ trap performances [16,17]. Cheng et al. focused on a systematic investigation towards the relationship between crystalline structures of MgAlFeCu mixed oxides and their SO$_2$ removal catalytic activity [18]. The mechanism of SO$_x$ trapping was studied in detail by Dathe et al. [19,20]. Although the SO$_2$ reactions on the surface of calcined hydrotalcite-like compounds have been studied widely, large uncertainties remain concerning the whole heterogeneous reaction, in particular, the formation and structure of sulfate because the interaction between SO$_2$ and the metal oxides surface is very complicated, depending on the nature of the adsorption sites. Therefore, a better understanding of the overall SO$_2$ transformation and the geometry of adsorbed sulfate on the metal oxides surface are highly desirable. *In situ* Fourier transform infrared spectroscopy (*In situ* FTIR) can provide information on reactive intermediates formed on the surface and is especially useful in exploring mechanisms of heterogeneous reactions of gases on a solid surface. Besides experimental investigations, a number of density functional theory (DFT) based calculations have been devoted to infer the structure of adsorbed sulfate on catalyst and to predict the interactions of adsorbates with catalytic sites [21–23].

* Corresponding author. Tel.: +86 411 8470 7733; fax: +86 411 8470 8084.
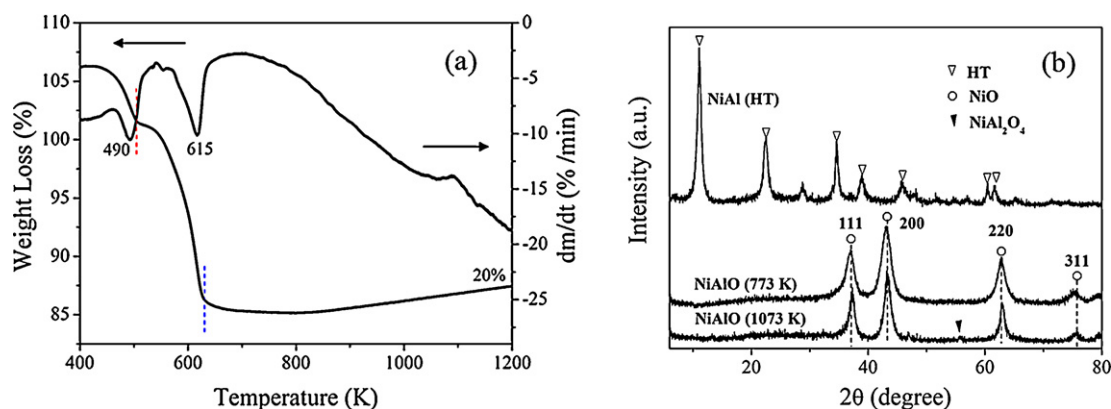*E-mail address:* xyli@dlut.edu.cn (X. Li).

Fig. 1. (a) TGA/DTG curves of NiAl hydrotalcite with the Ni/Al molar ratio of 3; (b) XRD patterns of the as-synthesized NiAl-HT sample and the NiAl mixed oxides.

2. Experimental

2.1. Materials

NiAl hydrotalcite was prepared by a urea hydrolysis method. 100 ml of deionized water, 20 ml of a metallic salts solution ($Ni^{2+} + Al^{3+} = 1$ mol/l, Ni/Al = 3) and urea (urea/($Ni^{2+} + Al^{3+}$) = 10) were added into a three-neck flask and stirred at 298 K. The flask was soaked in an oil bath previously heated at 363 K to start the hydrolysis reaction. The reaction was stopped by quenching it in a cold-water bath after 24 h under stirring. The precipitate was washed several times with absolute ethanol and deionized water and dried at 353 K overnight. The final product was calcined at 773 K for 4 h, and labeled as NiAlO.

2.2. Techniques of characterization

The obtained catalyst was characterized on a Rigaku D/Max 2550VB/PC X-ray powder diffractometer (XRD) with a Cu Kα radiation source ($k = 0.154056$ nm), and operated at a voltage of 40 kV and a current of 100 mA. Thermogravimetric analyses (TGA) were performed under air atmosphere, with a heating rate of 2 K/min in a thermobalance TA Instruments model Q500HR. Elemental analysis was performed using a Shimadzu ICPS-7500 inductively coupled plasma emission spectrometer. N_2 physisorption was performed on a Quantachrome Autosorb-1 instrument to study surface area, pore volume, and pore size distribution. Scanning electron microscopy (SEM) was performed on a JEOLJSM-6360LV microscope. Transmission electron microscopy (TEM) experiment was performed with the JEM-2000EX microscope, using an accelerating voltage of 100 kV. For the TEM analysis, the catalyst was dispersed in absolute alcohol by an ultrasonic bath and deposited on a Formvar coated 200 mesh Cu grid. X-ray photoelectron spectroscopy (XPS) data were recorded using a PerkinElmer PHI 5600 electron spectrometer using acrochromatic Al Kα radiation (1486.6 eV) with Ar⁺ sputtering to remove the surface layer of the sample. The binding energies and intensities were calculated after subtraction of a linear-type background from raw photoemission spectra. The special software PHI-MATLAB was used for data analysis. The SO_2-TPD experiments were carried out on a catalyst of 0.2 g using a mass spectrometer (Hiden HPR20) for on-line monitoring of the SO_2-TPD effluent gas. Prior to TPD procedure, the samples were pretreated at 773 K for 1 h in a flow of Ar and cooled down to room temperature. The samples were then exposed to a flow of 200 ppm $SO_2 + 5$ vol.% O_2/Ar (50 ml/min) for 1 h, followed by Ar purge for another 1 h. Finally, the temperature was raised to 1173 K in Ar flow (50 ml/min) at the rate of 10 K/min.

2.3. Activity test

The adsorption equilibrium isotherms of SO_2 were analyzed using a volumetric method at 298 K and 473 K [24]. The method is based on the mole balance of SO_2 gas in a closed system.

Herein it is also assumed that there was no chemical reaction occurs in the set-up. The experiment set-up used for the adsorption measurement is described below. The system was first evacuated by vacuum before each measurement. The sample (0.1 g) was put in the sample holder at the beginning of the measurement and heated to the required temperature. The temperature of the sample holder was kept constant throughout the measurement. When the measurement was started, 5% O_2 gas was firstly dosed into the supply bomb, and then SO_2 gas was dosed into the supply bomb, the pressures and temperatures of the supply bomb and sample holder were then recorded. A certain amount of SO_2 gas in the supply bomb was then dosed into the sample holder until the pressure in the sampler holder reached a certain level. The SO_2 in the sample holder was adsorbed by the sample until the equilibrium was reached. The pressures and temperatures of the supply bomb and sample holder were recorded when the equilibrium was reached. The process was repeated with increasing the pressure level in the sample holder step by step until the desired maximum pressure was reached. Each set of pressures and temperature was used to calculate the amount of SO_2 adsorbed by the sample at each pressure level in the sample holder. As the setup was a close system, the amount of SO_2 in each chamber could be calculated using the ideal gas law:

$$n = \frac{PV}{RT}, \tag{1}$$

where n is the amount of SO_2 in the chamber (mole), P is the pressure in the chamber (Pa), V is the volume of the chamber (m^3), R is the gas constant (8.314 Pa m³/(mol K)) and T is the temperature in the chamber (K).

As the volumes of the supply bomb and sample holder were fixed, with the pressure and temperature of the supply bomb and sample holder before and after each adsorption point, the amount of SO_2 gas in the system before and after each adsorption point can be calculated. The difference between the total amounts of SO_2 in the supply bomb and sample holder before and after each adsorption was the amount of SO_2 adsorbed by the sample at each pressure level. Thus, the adsorption capacity of the sample at each pressure level can be estimated. By plotting the adsorption capacity against the pressure in the sample holder, an adsorption isotherm of the sample could be obtained.

Table 1
Chemical composition and structural parameters of calcined NiAlO catalyst.

Sample	Ni:Al atomic ratio[a]	S_{BET}[b] (m^2/g)	Total volume[c] (cm^3/g)	Pore diameter[d] (nm)
NiAlO	2.87	143	0.40	6.4

[a] Ni:Al atomic ratios are calculated from ICP analysis.
[b] BET surface area calculated from the linear part of the BET plot.
[c] Single-point total pore volume of pores at $P/P_0 = 0.99$.
[d] Estimated using the desorption branch of the isotherm.

2.4. In situ FTIR experiment

FTIR spectra were recorded on a VERTEX 70-FTIR equipped with a smart collector. The catalyst (approximately 20 mg) was prepared by pressing it into a pallet and then secured inside the infrared cell, which consists of two KBr windows and a sample holder for the catalyst pallet. The infrared cell is connected to a vacuum chamber through a Teflon tube and a glass gas manifold with ports for gas introduction and a vacuometer. Prior to each experiment, the catalyst was first heated for 60 min at 673 K, and then cooled to the desired temperature. The background spectrum was recorded with the flowing of $O_2 + N_2$ and was subtracted from the catalyst spectrum. All spectra were measured with a resolution of $4 \, cm^{-1}$ and with an accumulation of 100 scans. All the measurements were repeated at least twice.

2.5. Theoretical

DFT calculations were performed to estimate the structure of surface sulfate species formed on NiAl mixed oxide. The Gaussian 03 program [25] running on a Dell OPTIPLEX 380 with a Pentium (R) Dual-Core, 2.70 GHz Processor and 1 G RAM was performed to optimize the structures and calculate the vibrational wavenumbers for the calculated models. The hybrid Becke 3–Lee–Yang–Parr (B3LYP) exchange-correlation functional with the 6-31G* basis set were employed [26,27]. The vibrational frequencies and intensities for the calculated models were analyzed by the Gaussview 3.09 program package. Calculated frequencies were corrected by a scaling factor of 0.9613 [28,29] and compared with experimentally observed vibrational frequencies.

3. Results and discussion

3.1. Characterizations

Typical TGA and DTA curves of the hydrotalcite NiAl are illustrated in Fig. 1a. The total weight loss percentage oscillates is about 20 wt%. The TGA result shows an initial reduction in weight between room temperature (RT) and 500 K arising from physisorbed and interlayer water [30]. A second weight loss between 500 and 620 K results from a concomitant dehydroxylation of the laminae and expulsion of the nitrate and carbonate anions located in the interlayer region in the form of CO_2 and NO_x [31]. Beyond 620 K, the calcined NiAl-HTs catalyst presents the better thermal stability. The corresponding DTG curve shows two main effects associated with these weight losses. The first endothermic peak is 490 K and the second one is 615 K. Thus, we chose 773 K as a proper calcination temperature for the preparation of the NiAlO. The XRD patterns of the as-synthesized and calcined NiAl-HT catalysts are illustrated in Fig. 1b. Before calcination, the catalyst showed the characteristic diffraction corresponding to hydrotalcite-like structure [32,33]. The patterns were recorded over a range of 2θ angles from 5° to 80° and the crystalline phases were identified using the Joint Committee on Powder Diffraction Standards (JCPDS) files. After calcination at 773 K, the NiAlO catalyst shows four distinctive peaks at $2\theta = 37.4°, 43.0°, 63.4°$ and $75.2°$,

which are corresponding to the NiO (1 1 1), (2 0 0), (2 2 0) and (3 1 1) crystal planes (JCPDS 47-1049), respectively. The results indicate that the hydrotalcite layered structure has completely collapsed due to the removal of structural H_2O and CO_2 from the interlayer, and this mixed oxide presents the pattern of pure NiO. When the temperature of calcination reaches 1073 K, a small amount of $NiAl_2O_4$ spinel is detected, characterized by the peaks at 55° (JCPDS 78-1601). No diffraction peaks corresponding to crystalline Al phase can be observed, owing to the good dispersion of Al species in the oxide matrices.

The Ni/Al atomic ratio in the calcined NiAlO catalyst is calculated from ICP results, as listed in Table 1. No obvious difference was found between the Ni/Al atomic ratio in the calcined catalyst and that in the starting mixed solution, suggesting that the hydrotalcite-like NiAl compounds can be successfully prepared. This is in good accordance with the XRD results of the corresponding precursor.

SEM analysis of NiAlO shows a flower-like hierarchical structure, whose size is in the range between 1 and 2 μm. The structure is comprised of densely packed irregular nano flakes with the size of ca.10–30 nm (Fig. 2a). Further insight into the morphology was gained using TEM. The image (Fig. 2b) shows that the formation of thin flat plates irregular in size and shape, with a ribbon-like appearance which probably is formed by overlapped interaction among them (indicated by the arrows Fig. 2b).

The textural parameters of the NiAlO catalyst are listed in Table 1. The BET specific surface area, pore volume and average pore size are $143 \, m^2/g$, $0.40 \, cm^3/g$ and 6.4 nm, respectively.

3.2. Adsorption of SO_2

Fig. 3a shows the adsorption isotherms of SO_2 onto NiAlO catalyst at 298 K and 473 K. The two isotherms are both of type I, which means the adsorption capacity is higher at the low P/P_0 region. A Type I isotherm is generally characterized as having an adsorption plateau at higher pressures. This plateau is generally associated with saturation. For the case presented here, the measured SO_2 adsorption increases with pressure at low relative pressure (e.g. $P/P_0 < 0.01$); however, at higher pressures the trend eases, and a plateau is reached. The maximum SO_2 adsorption capacities are 0.65 and 0.58 mmol/g corresponding to 298 K and 473 K, respectively. Specifically, significant differences were observed between the regions before and after $P/P_0 = 0.01$. At lower SO_2 concentrations ($P/P_0 < 0.01$), the moles of adsorbed SO_2 increased very fast and were independent of the adsorption temperature. Conversely, in the region of $P/P_0 > 0.01$, higher adsorption temperatures gave lower amount of SO_2 at the same concentration, and SO_2 amount increased with SO_2 concentration up to about 0.1% SO_2 at similar adsorption temperatures.

3.3. TPD Analysis

An example of a SO_2-TPD experiment for NiAlO catalyst is illustrated in Fig. 3b after exposure to 200 ppm $SO_2 + 5$ vol.% O_2 in He for 1 h at 298 K. The SO_2 (m/z = 64) signal was monitored. In order to understand the surface species better, the TPD graph was fitted using Lorenz and Gaussian curves as shown in Fig. 3b with a
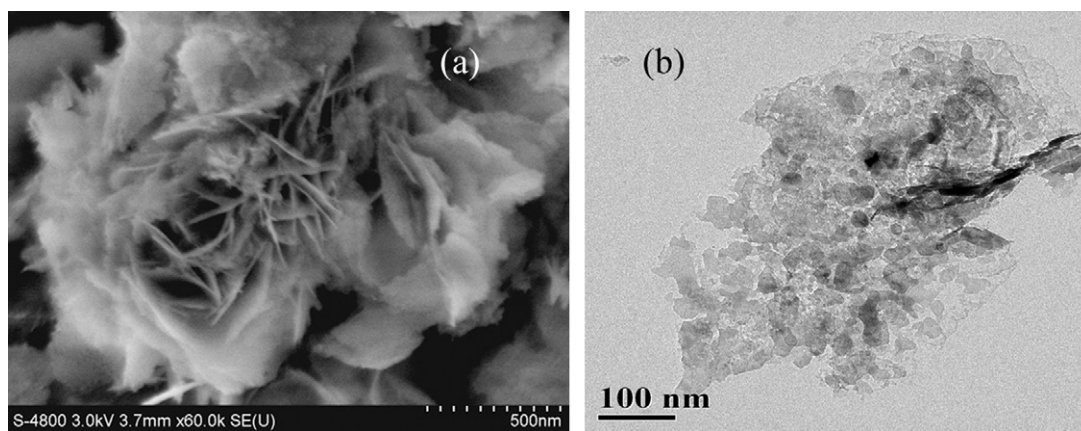
Fig. 2. (a) SEM image of calcined NiAlO catalyst; (b) TEM image of calcined NiAlO catalyst.

correlation coefficient of 0.991. There are five distinct peaks centered at 370, 480, 630, 900 and 1000 K, respectively. The peaks at 370 and 480 K were assigned to the desorption of molecular SO_2 from NiAlO surface [34,35]. Two overlapping SO_2 desorption features were observed between 850 and 1100 K. According to the previous literature [36,37], the higher temperature peak centered around 1000 K should be derived from the thermally stable sulfate compounds formed on the Al–O site, while the lower temperature peak (900 K) should be attributed to SO_2 decomposed from the sulfate species formed on the Ni–O site. The TPD results provide clear evidence for the formation of sulfate species by the reaction of NiAlO catalyst with $SO_2 + O_2$. In addition, on the basis of previous studies [38], we suggest that the peaks centered at 630 K are associated with the decomposition of surface sulfite.

3.4. X-ray photoelectron spectra of NiAlO catalysts surfaces

XPS scans recorded in the S_{2p} region taken from NiAlO before and after its interaction with sulfur dioxide are shown in Fig. 3c. No S signals (Fig. 3c(A)) can be identified, indicating that there is no sulfur species before the reaction. Two species are observed on the surface after reaction in the S_{2p} with characteristics S_{2p} doublets ($S_{2p3/2}$ and $S_{2p1/2}$) present in a 2:1 ratio and with an energy difference of 1.2 eV. The first species can be assigned to surface bound sulfite with an $S_{2p3/2}$ binding energy of 168.7 eV. The other new species at an $S_{2p3/2}$ value of 170 eV, is ascribed to the sulfate species. The values we observe for the sulfite and sulfate binding energy were within the range of values reported in the literature [39,40]. Additionally, the relative concentration ratio of $[SO_3{}^{2-}]$ to $[SO_4{}^{2-}]$ is 27:73, which is calculated from the peak area of the corresponding species on the XPS spectra. This result indicates that 27% of the total gas-phase SO_2 adsorbed on the surface of NiAlO

was converted to $SO_3{}^{2-}$. The rest (about 73%) existed in the form of the species $SO_4{}^{2-}$. Therefore, the calcined NiAlO catalyst contained a certain amount of both sulfite and sulfate species after adsorption of SO_2. The present XPS results corroborate the TPD results and further support the idea that the sulfate species was formed on the NiAlO catalyst surface.

3.5. In Situ FTIR spectra of SO_2 adsorption on the NiAlO catalyst

To investigate the interaction between $SO_2 + O_2$ and the NiAlO catalyst, *in situ* FTIR experiments were conducted to figure out the adsorption pathways and to analyze the nature of the sulfate species on the NiAlO catalyst. The catalyst was exposed to a flow of $SO_2/O_2/N_2$ (200 ppm SO_2, 5 vol.%O_2, and N_2 as balance) at 298 K and 473 K for 10 min respectively, and then the inlet and outlet were closed. The adsorption behaviors of the catalysts at 298 K and 473 K are similar to each other, so only the results of the two catalysts at 473 K are chosen as the representative, as illustrated in Fig. 4a. The peak at 1632 cm^{-1} is assigned to the δ (HOH) of adsorbed H_2O [41]. It is evident that the intensities of the negative peak at 3702 cm^{-1} increased with time. This band is attributed to the vibrations of the surface hydroxyl species (OH) [42]. The negative features indicate either consumption of hydroxyl groups from the surface or that the hydroxyl groups are involved in hydrogen bonding during the reaction. Several new bands at 1457, 1227, 1139, 1049, 980 and 925 cm^{-1} were detected, and the intensity increased with time until the surface was saturated. All of these peaks are also assigned to sulfur containing species. The bands at 1049, 980 and 925 cm^{-1} could be assigned to the stretching motion of surface-coordinated bisulfite and/or sulfite. The results agree well with other infrared studies reported previously [43–47]. Mitchel et al. [44], John et al. [46], and Goodman et al. [43] investigated SO_2
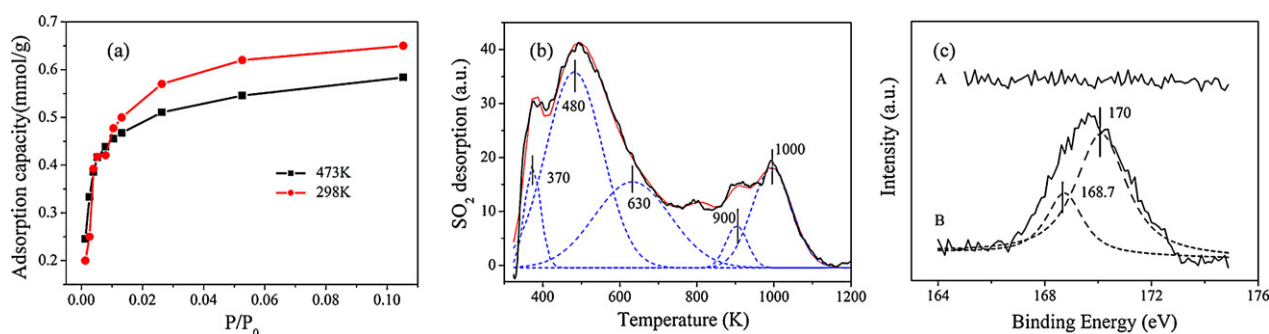

Fig. 3. (a) Adsorption equilibrium isotherms of SO_2 in the calcined NiAlO catalyst at 298 and 473 K; (b) SO_2 TPD profiles of fresh NiAlO catalyst; (c) XPS spectra of $S_{2p3/2}$ on the NiAlO catalyst before A and after B reaction with $SO_2 + O_2$.

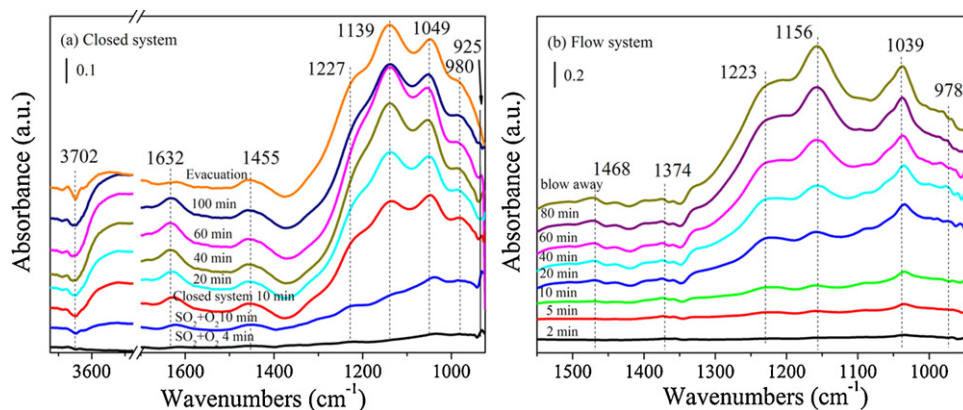**Fig. 4.** (a) Dynamic changes of *in situ* FTIR spectra for NiAlO catalyst at 473 K after relation with $SO_2 + O_2$ in closed system; (b) Dynamic changes of *in situ* FTIR spectra for NiAlO catalyst at 473 K after relation with $SO_2 + O_2$ in flow system.
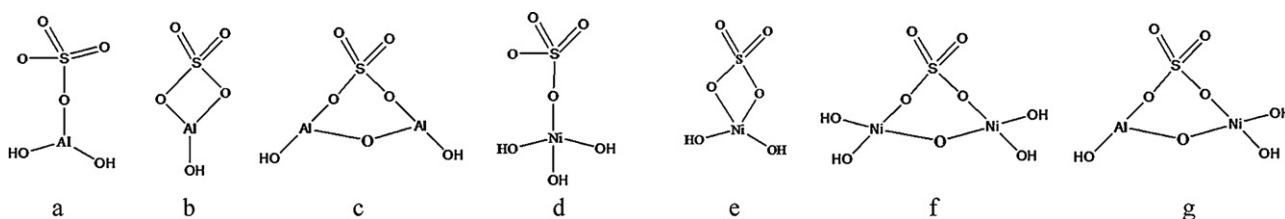

Fig. 5. Calculated models for the sulfate species formed on NiAlO model clusters: (a) MNMD binding geometry for $Al(O_x)$; (b) MNBD binding geometry for $Al(O_x)$; (c) BNBD binding geometry for $Al(O_x)$; (d) MNMD binding geometry for $Ni(O_x)$; (e) MNBD binding geometry for $Ni(O_x)$; (f) BNBD binding geometry for $Ni(O_x)$; (g) BNBD binding geometry for $NiAl(O_x)$.

adsorption on γ-Al_2O_3 particles and found that the broad band centered at $1060\,cm^{-1}$ was assigned to strongly adsorbed SO_2 identified as a sulfite species. Martin et al. [47] studied reaction of SO_2 on CaO particles. Upon reaction of SO_2 on CaO, they observed a broad absorption band centered at $950\,cm^{-1}$ and assigned this band to the $\nu3$ and $\nu1$ stretching modes of surface sulfite. Schoonheydt and Lunsford also reported surface sulfite absorption bands at 975 and $1040\,cm^{-1}$ following reaction of SO_2 on MgO at room temperature [45]. Additionally, according to previous studies [47–49], the bands at 1227, 1139, $1049\,cm^{-1}$ match well with the stretching motion of adsorbed sulfate on the surface of the catalysts. The relationship between the symmetry of sulfate complexes and their infrared spectra has been well established [50,51]. According to the theory, there were two infrared sulfate vibrations that were accessible to FTIR investigation, which were the non-degenerate symmetric stretching $\nu1$ band and the triply degenerate asymmetric stretching $\nu3$ band. When the bidentate sulfate complex was formed on the surface of the catalyst, the $\nu3$ band would split into three bands between 1250 and $1050\,cm^{-1}$. More specifically, the bidentate sulfate could still be divided into the bidentate binuclear sulfate and the bidentate mononuclear sulfate. In the case of a bidentate binuclear sulfate, the typical three split $\nu3$ bands of bidentate binuclear sulfate were between 1050 and $1250\,cm^{-1}$. If the bidentate mononuclear sulfate was formed, the bands would shift to higher wavenumbers [50]. Thus, on the basis of the discussion above, the main production of SO_2 adsorption was the bidentate binuclear sulfate in our work. The peak located at $1049\,cm^{-1}$ could be attributed to the cooperative effects of surface sulfite and sulfate. In addition, according to previous studies [51], the band at $1457\,cm^{-1}$ can be attributed to SO_3 species.

To gain further information about the reaction of SO_2 on the NiAlO catalyst, *in situ* FTIR spectra of the NiAlO sample as a function of time was measured in a flow of $SO_2 + O_2$ for a total of 80 min at 473 K (Fig. 4b). Several new bands at 1465, 1374, 1223, 1156, 1039 and $978\,cm^{-1}$ were detected obviously, and the intensity increased

with time until the surface was saturated. Similar to Fig. 4a, the bands at 1039 and $978\,cm^{-1}$ could be assigned to the stretching motion of surface-coordinated bisulfite and/or sulfite [43–47]. The bands at 1374, 1223 and $1156\,cm^{-1}$ could be assigned as the stretching motion of adsorbed sulfate [43–47]. In addition, the band at $1465\,cm^{-1}$ can be attributed to SO_3 species [51].

3.6. DFT vibrational frequency calculation and identification of adsorbed complexes

To obtain a better understanding of the coordination geometry of the adsorbed complexes, infrared vibrational frequencies were calculated. The positions of Ni, Al and O atoms were optimized in the DFT calculations using Gaussian 03 program. They are greatly the same as the surface morphology of the real NiAl catalyst. The designed composite metal oxide cluster models represent the surface morphology of the real NiAl catalyst. Furthermore, vibrational frequencies were calculated for sulfate species individually in three different possible binding geometries: (a) mononuclear monodentate (MNMD), (b) mononuclear bidentate (MNBD) and (c) binuclear bidentate (BNBD) [28,52]. Moreover, numerous experimental and computational studies have demonstrated that sulfate species were mostly formed on the surface of mixed oxides catalysts. For these reasons above, we designed seven kinds of calculated models containing $Al(O_x)$, $Ni(O_x)$ and $NiAl(O_x)$ on the surface of NiAlO cluster to obtain a better analysis of the nature of the sulfate species and to explain the phenomenon for the *in situ* FTIR spectra. These adsorption geometries are depicted in Fig. 5. The optimized structures are presented in Fig. 6. Calculated frequencies are listed in Table 2. Fig. 7 displays a plot of calculated *versus* experimental frequencies for the seven different adsorption geometries. Among these adsorption geometries, the plot suggests that the model *c* (BNBD binding geometry for $Al(O_x)$), model *f* (BNBD binding geometry for $Ni(O_x)$) and model *g* (BNBD binding geometry for $NiAl(O_x)$) have better correlation with our experimentally determined
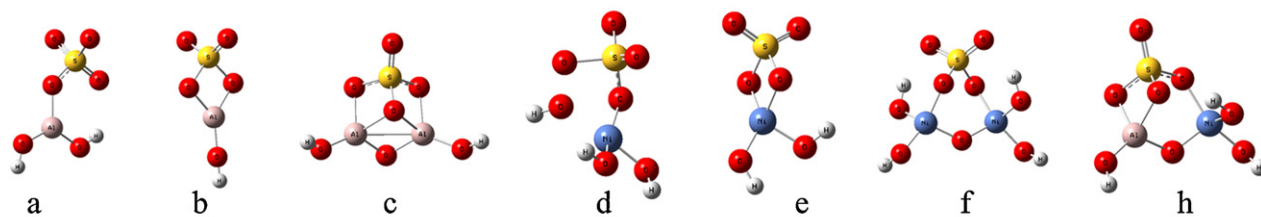
Fig. 6. Optimized configuration of calculational models for the sulfate species formed on NiAlO model clusters: (a) MNMD binding geometry for Al(O$_x$); (b) MNBD binding geometry for Al(O$_x$); (c) BNBD binding geometry for Al(O$_x$); (d) MNMD binding geometry for Ni(O$_x$); (e) MNBD binding geometry for Ni(O$_x$); (f) BNBD binding geometry for Ni(O$_x$); (g) BNBD binding geometry for NiAl (O$_x$).

Table 2
Comparisons of observed and calculated frequencies (cm^{-1}) for the geometry-optimized models.

Modes	Observed frequencies (cm^{-1})	Calculated frequencies (cm^{-1})						
		a	b	c	d	e	f	g
ν_s (OSO)	980, 925	901	870	916	848	800	911	992
ν_{as} (OSO)	1049	NA	NA	1060	NA	NA	NA	1072
ν_s (S=O)	1139	1089	1142	NA	1211	1194	1143	NA
ν_{as} (S=O)	1227	1158	1411	1383	1413	1412	1357	1380
ν (OH) (surface hydroxyl)	3702	3690	3848	3723	3473	3512	3512	3738
R^2	NA	0.991	0.992	0.995	0.985	0.983	0.994	0.998
Standard deviation	NA	112.14	142.34	90.21	173.68	194.56	110.13	9.45
Y-intercept	NA	−38.96	−38.10	30.23	143.63	93.50	80.45	67.03

frequencies based on an analysis of the slope, standard deviation, and R^2 correlation of the different plots (see Table 2). The models c, f and g are associated with the better R^2 correlation (0.995, 0.994 and 0.998). We infer from this analysis that adsorbed sulfate species likely adopts a BNBD binding configuration on the surface of NiAlO catalyst. These DFT calculations results are in agreement with prior *in situ* FTIR experimental studies that proposed mainly a bidentate binuclear sulfate binding geometry formed on NiAlO surface after SO$_2$ adsorption.

3.7. Possible mechanism of the reactions of SO$_2$ on the NiAlO surface

The adsorption process of SO$_2$ is the cooperative physisorption and chemisorption. The physisorption capacity is determined by
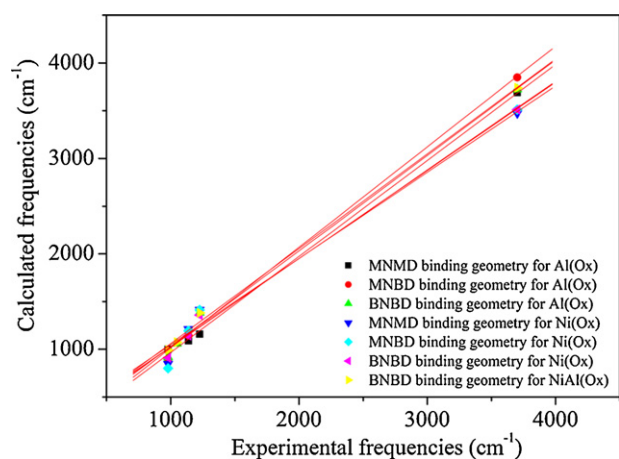

Fig. 7. Linear regression plots that compare experimentally determined to calculated vibrational frequencies for the different geometries in Fig. 5. Linear fit parameters are given in Table 2. On the basis of this analysis, the more probable coordination geometry of the sulfate species formed on NiAlO model clusters are BNBD binding geometry for Al(O$_x$), BNBD binding geometry for Ni(O$_x$) and BNBD binding geometry for NiAl (O$_x$).

the surface area and number of pores on the adsorbent substrate. Mixed oxides prepared from the hydrotalcites have higher surface areas and they are rich in pores. This may be one reason why calcined hydrotalcites have a better adsorption capacity of SO$_2$. The chemisorption capacity is related with the oxides surface basicity sites. This is quite understandable because these basic sites are involved as the reactive sites in this reaction. Jame and William elaborated that adsorption of SO$_2$ on Lewis base sites (exposed oxygen atoms) were prone to a strong interaction and followed by rearrangement where the sulfite species attached to the metal atom through the sulfur atom resulted in chemisorbed sulfate [53]. Karge and Dalla Lana further developed this theory [54]. They determined that the interaction of SO$_2$ with basic sites on the surface of γ-Al$_2$O$_3$ led to the formation of chemisorbed SO$_2$. Pacchioni et al. conducted a theoretical study of the adsorption and reaction of SO$_2$ on clean, completely dehydroxylated MgO surfaces. It was suggested that sulfite could be formed by interaction of the sulphur atom in SO$_2$ with two surface five-coordinated O^{2-} anions [55]. Chen and co-workers observed that the formation of the surface coordinated sulfite could be due to the interaction of SO$_2$ with four-coordinated O^{2-} anions while MgO particles reacted with SO$_2$ [56]. For NiAl mixed oxide from hydrotalcite-like precursors, which has a structure similar to MgO, the sites for SO$_2$ adsorption are expected to associate with O^{2-}–Ni^{2+} (or Al^{3+}) sites. During SO$_2$ sorption, the acidic SO$_2$ reacts with basic O^{2-} sites depending on their coordination (Fig. 8). Oxygen atoms located at edges and corners of the crystal planes which have stronger basicity than oxygen atoms in basal planes, are more important for SO$_2$ adsorption.

Thus, we propose the following possible mechanism of the reaction of SO$_2$ on NiAlO catalysts, as shown in Fig. 9. At first SO$_2$ could be weakly adsorbed on the surface of the NiAlO particles, while SO$_2$ could interact with the surface hydroxides or O^{2-} anions on the surface of the NiAlO particles, forming the surface-coordinated SO$_3^{2-}$/HSO$_3^-$ and SO$_4^{2-}$. *In situ* FTIR results have provided the evidence for the formation of adsorbed SO$_3^{2-}$/HSO$_3^-$ and SO$_4^{2-}$, and the direct consumption of hydroxyl groups (Fig. 4). Furthermore, more O^{2-} (sites) would become available because of OH consumption, and this could well explain the phenomenon for *in situ* FTIR spectra that the bands of adsorbed SO$_2$ speciation remained
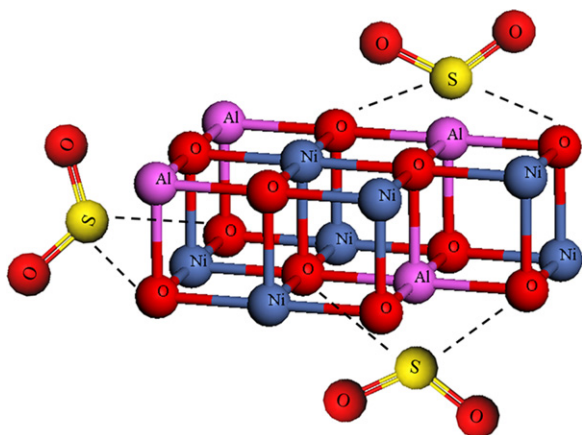
Fig. 8. The basic sites are important for SO$_2$ adsorption.
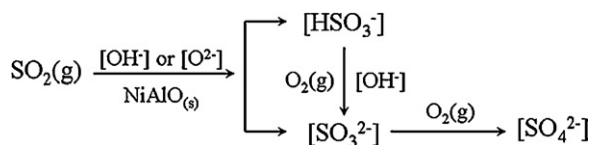

Fig. 9. Possible reaction mechanism of SO$_2$ over the calcined NiAlO catalyst.

increasing after the OH groups stopped loss. When the O^{2-} anions are consumed, O$_2$ in the gas-phase can supplement it so that the oxidation reaction can continue until the surface is fully covered by surface SO$_3^{2-}$, HSO$_3^-$ and SO$_4^{2-}$ species.

4. Conclusions

The hydrotalcite-based NiAl mixed oxides have the property of SO$_2$ adsorption both at room temperature and higher temperature (473 K). The prepared NiAlO showed the excellent SO$_2$ adsorption and the adsorption equilibrium of SO$_2$ was a type I isotherm, which significantly improves the adsorption performance for low-concentration SO$_2$. *In situ* FTIR revealed that surface bisulfite, sulfite, and bidentate binuclear sulfate were formed on calcined NiAlO catalyst as the products of reaction with SO$_2$ + O$_2$. DFT based computations and the vibration frequency calculations confirmed that sulfate species adopted a binuclear bidentate binding configuration on the surface of NiAlO catalyst. This work provides a fundamental understanding on the mechanism of SO$_2$ catalytic oxidation over NiAl hydrotalcite-based mixed oxides. Further studies to explore the performances for SO$_2$ removal by catalytic oxidation under real environmental conditions are under progress.

Acknowledgments

References

[1] M.R. Othman, Z. Helwani, M. Martunus, W.J.N. Fernando, Appl. Organomet. Chem. 23 (2009) 335–346.

[2] F. Cavani, F. Trifiró, A. Vaccari, Catal. Today 11 (1991) 173–301.
[3] P.S. Braterman, Z.P. Xu, F. Yarberry, Chemistry of layered double hydroxides, in: Handbook of Layered Materials, Marcel Dekker, New York, 2004.
[4] D.G. Evans, X. Duan, Chem. Commun. 5 (2006) 485–496.
[5] F. Leroux, C. Taviot-Gueho, J. Mater. Chem. 15 (2005) 3628–3641.
[6] J.H. Choy, Ceram. Trans. 190 (2006) 213–225.
[7] Y. Yajima, J.G. Li, T. Ikegami, J.H. Lee, T. Mori, Ceram. Int. 27 (2001) 481–489.
[8] G. Hu, Z. Sun, H. Gao, Environ. Sci. Technol. 44 (2010) 6712–6717.
[9] T. Raju, S.J. Chung, I.S. Moon, Environ. Sci. Technol. 42 (2008) 7464–7469.
[10] C. Wang, H. Liu, X.Z. Li, J.Y. Shi, G. Ouyang, M. Peng, C.C. Jiang, H.N. Cui, Environ. Sci. Technol. 42 (2008) 8585–8590.
[11] Y.Z. Li, H.L. Dong, Y. Li, X.C. Xu, Environ. Sci. Technol. 41 (2007) 2894–2900.
[12] J.S. Yoo, A.A. Bhattacharyya, C.A. Radlowski, J.A. Karch, Appl. Catal. B: Environ. 1 (1992) 169–189.
[13] A. Corma, A.E. Palomares, F. Rey, Appl. Catal. B: Environ. 4 (1994) 29–42.
[14] M. Cantu, E. Lopez-Salinas, J.S. Valente, R. Montiel, Environ. Sci. Technol. 39 (2005) 9715–9720.
[15] A.E. Palomares, J.M. López-Nieto, F.J. Lázaro, A. López, A. Corma, Appl. Catal. B: Environ. 20 (1999) 257–266.
[16] G. Centi, S. Perathoner, Appl. Catal. B: Environ. 70 (2007) 172–178.
[17] G. Centi, S. Perathoner, Catal. Today 127 (2007) 219–229.
[18] W.P. Cheng, J.G. Yang, M.Y. He, Catal. Commun. 10 (2009) 784–787.
[19] H. Dathe, A. Jentys, J.A. Lercher, Phys. Chem. Chem. Phys. 7 (2005) 1283–1292.
[20] H. Dathe, P. Haider, A. Jentys, J.A. Lercher, J. Phys. Chem. B 110 (2006) 10729–10737.
[21] C. Maurizio, F. Francesca, M. Chiara, V. Andrea, J. Phys. Chem. B 109 (2005) 12596–12602.
[22] K.M. Eida, H.Y. Ammarb, Appl. Surf. Sci. 257 (2011) 6049–6058.
[23] M.J. Harrison, D.P. Woodruff, J. Robinson, Surf. Sci. 9 (2006) 1827–1836.
[24] X. Hu, B. King, D.D. Do, Gas Sep. Purif. 8 (1994) 187–190.
[25] M. Frisch, J. Foresman, A. Frisch, Gaussian 98, Gaussian Inc., Pittsburgh, PA, 1998.
[26] A.D. Becke, J. Chem. Phys. 98 (1993) 5648–5652.
[27] V.A. Rassolov, M.A. Ratner, J.A. Pople, P.C. Redfern, L.A. Curtiss, J. Comput. Chem. 22 (2001) 976–984.
[28] T.H. Yoon, S.B. Johnson, C.B. Musgrave, G.E. Brown, Geochim. Cosmochim. Acta 68 (2004) 4505–4518.
[29] M.W. Wong, Chem. Phys. Lett. 256 (1996) 391–399.
[30] J.S. Valente, M.S. Cantú, J.G.H. Cortez, R. Montiel, X. Bokhimi, E. López-Salinas, J. Phys. Chem. C 111 (2007) 642–651.
[31] L. Chmielarz, P. Kustrowski, A. Rafalska, R. Dziembaj, Thermochim. Acta 395 (2002) 225–236.
[32] D.G. Cantrell, L.J. Gillie, A.F. Lee, K. Wilson, Appl. Catal. A: Gen. 287 (2005) 183–190.
[33] Y. Cesteros, P. Salagre, F. Medina, J.E. Sueiras, Appl. Catal. B: Environ. 25 (2000) 213–227.
[34] W.Q. Xu, H. He, Y.B. Yu, J. Phys. Chem. C 113 (2009) 4426–4432.
[35] W. Chen, Y. Jiang, W. Li, R. Jin, S. Tang, W. Hu, Catal. Today 50 (1999) 39–41.
[36] Q. Wu, H.W. Gao, H. He, J. Phys. Chem. B 110 (2006) 8320–8324.
[37] Q.X. Ma, Y.C. Liu, H. He, J. Phys. Chem. A 112 (2008) 6630–6635.
[38] S.H. Overbury, D.R. Mullins, D.R. Huntley, L. Kundakovic, J. Phys. Chem. B 103 (1999) 11308–11317.
[39] M.Y. Smirnov, A.V. Kalinkin, A.V. Pashis, A.M. Sorokin, A.S. Noskov, K.C. Kharas, V.I. Bukhtiyarov, J. Phys. Chem. B 109 (2005) 11712–11719.
[40] D.I. Sayago, P. Serrano, O. Böhme, A. Goldoni, G. Paolucci, E. Roman, J.A. Martin-Gago, Surf. Sci. (2001) 482–485.
[41] J.F. Liu, Y.B. Yu, Y.J. Mu, H. He, J. Phys. Chem. B 110 (2006) 3225–3230.
[42] J.B. Peri, J. Phys. Chem. 69 (1965) 220–230.
[43] A.L. Goodman, P. Li, C.R. Usher, V.H. Grassian, J. Phys. Chem. A 105 (2001) 6109–6120.
[44] M.B. Mitchell, V.N. Sheinker, M.G. White, J. Phys. Chem. 100 (1996) 7550–7557.
[45] R.A. Schoonheydt, J.H. Lunsford, J. Catal. 26 (1972) 261–271.
[46] M.H.L. John, Z. Tom, C. Peter, J. Phys. Chem. C 114 (2010) 10444–10454.
[47] M.A. Martin, J.W. Childers, R.A. Palmer, Appl. Spectrosc. 41 (1987) 120–126.
[48] Y. Lee, J. Park, Environ. Sci. Technol. 36 (2002) 1086–1092.
[49] C. Quijada, A. Rodes, J.L. Vazquez, J.M. Perez, A. Aldaz, J. Electroanal. Chem. 394 (1995) 217–227.
[50] D. Peak, R.G. Ford, D.L. Sparks, J. Colloid Interface Sci. 218 (1999) 289–299.
[51] B.Q. Jiang, Z.B. Wu, Y. Liu, S.C. Lee, W.K. Ho, J. Phys. Chem. C 114 (2010) 4961–4965.
[52] K. Axe, M. Vejgarden, P. Persson, J. Colloid Interface Sci. 294 (2006) 31–37.
[53] W. James, F.B. William, Thermochim. Acta 288 (1996) 179–189.
[54] H.G. Karge, I.G. Dalla Lana, J. Phys. Chem. 88 (1984) 1538–1543.
[55] G. Pacchioni, A. Clotet, J.M. Ricart, Surf. Sci. 315 (1994) 337–346.
[56] X.Y. Zhang, G.S. Zhuang, J.M. Chen, Y. Wang, X. Wang, Z.S. An, P. Zhang, J. Phys. Chem. B 110 (2006) 12588–12596.